Motivated by our analysis, we have explored other implementations of the CSAR concept. The echo-to-echo propagator of a single refocusing sequence shown in Fig. 3B is to first order a rotation by 2π rather than π. Therefore, we expect refocusing of both even and odd echoes. This refocusing was seen experimentally with a slight even-odd modulation. The sequence consists of two subcycles, each composed of a nonadiabatic reversal of field B_B sandwiched between two adiabatic 180° rotations. Although the sequence is superior to the basic nonresonant sequence (Fig. 1B), the later echoes show an enhanced decay because the observed magnetization comes mainly from components perpendicular to $\hat{n}$. Finite reversal times lead to deviations of the rotation angle from the perfect 2π rotations that accumulate rapidly over several refocusing cycles.

These results suggest that the enhanced decay can be reduced by the use of a technique inspired by the broadband inversion techniques in resonant NMR, which use supercycles of rf phases (*25*, *26*) to compensate progressively for higher-order imperfections and inhomogeneities of rf and static fields. Instead of controlling the phase of rf pulses, we have the ability in nonresonant NMR to change the sense of the adiabatic rotations. Such a technique has been implemented in Fig. 3C. The sequence is based on the refocusing unit of the sequence in Fig. 3A and incorporates a four-unit supercycle of different senses of adiabatic rotation. The results show large amplitudes for echoes 4, 8, 12, and so on and slightly smaller ones for echoes 1, 5, 9, and so on, with a much smaller initial decay rate than the other sequences. The perturbative nature of the average Hamiltonian theory is particularly useful for the design of sequences with superior performance at early echoes (*25*, *26*). However, for increased echo numbers, the observed decay rate is still much higher than the intrinsic relaxation rate, and an approach based on the effective rotation-axis method is better suited to find sequences for T_2 measurements.

The nonresonant NMR methods described here require fast switching of applied fields that are sufficiently large, as compared to the background field, to achieve field reversal. These factors limit the sensitive volume achievable in practical ex situ applications, where fields weaken with distance. Although it appears to be impractical to employ the rather low magnetic fields of nonresonant NMR to perform chemical shift analyses, the CSAR sequences can be extended to include segments of pulsed-field gradients to perform imaging in a manner similar to conventional magnetic resonance imaging. The technique has further potential applications in multinuclei detection.

References and Notes

1. R. Muthupillai *et al.*, *Science* **269**, 1854 (1995).
2. C. F. Jenner, Y. Xia, C. D. Eccles, P. T. Callaghan, *Nature* **336**, 399 (1988).
3. M. J. McCarthy, *Magnetic Resonance Imaging in Foods* (Chapman & Hall, New York, 1994).
4. W. P. Halperin, F. D'Orazio, S. Bhattacharja, J. C. Tarczon, in *Molecular Dynamics in Restricted Geometries*, J. Klafter, J. Drake, Eds. (Wiley, New York, 1989), pp. 311–350.
5. J. F. Stebbins, I. Farnan, *Science* **245**, 257 (1989).
6. Y.-Q. Song, S. Ryu, P. N. Sen, *Nature* **406**, 178 (2000).
7. R. L. Kleinberg, "Well logging," in *Encyclopedia of Nuclear Magnetic Resonance* (Wiley, Chichester, UK, 1996), vol. 8, pp. 4960–4969.
8. G. Eidmann, R. Savelsberg, P. Blümler, B. Blümich, *J. Magn. Reson. A* **122**, 104 (1996).
9. M. D. Hürlimann, D. D. Griffin, *J. Magn. Reson.* **143**, 120 (2000).
10. C. A. Meriles, D. Sakellariou, H. Heise, A. J. Moulé, A. Pines, *Science* **293**, 82 (2001).
11. M. H. Levitt, "Composite pulses," in *Encyclopedia of Nuclear Magnetic Resonance* (Wiley, Chichester, UK, 1996), vol. 2, pp. 1396–1411.
12. M. Garwood, L. DelaBarre, *J. Magn. Reson.* **153**, 155 (2001).
13. M. E. Packard, R. Varian, *Phys. Rev.* **93**, 941 (1954).
14. A. Abragam, *Principles of Nuclear Magnetism* (Clarendon, Oxford, UK, 1978).
15. R. McDermott *et al.*, *Science* **295**, 2247 (2002).
16. M. D. Hürlimann, Y.-Q. Song, S. Ryu, P. N. Sen, U.S. Patent 6,133,735 (October 2000).
17. B. F. Melton, V. L. Pollack, *Rev. Sci. Instrum.* **42**, 769 (1971).
18. R. N. Chandler, W. E. Kenyon, C. E. Morriss, *Transactions of the 28th Annual SPWLA Logging Symposium,* London, England, 29 June to 2 July, 1987, vol. 1, (SPWLA, Houston, TX, 1987), pp. C1–C25.
19. D. J. Sloop, T.-S. Lin, J. J. H. Ackerman, *J. Magn. Reson.* **139**, 60 (1999).
20. E. L. Hahn, *Phys. Rev.* **80**, 580 (1950).
21. I. Solomon, *Phys. Rev. Lett.* **2**, 301 (1959).
22. M. V. Berry, *Proc. R. Soc. London Ser. A* **392**, 45 (1984).
23. J. W. Zwanziger, M. Koenig, A. Pines, *Annu. Rev. Phys. Chem.* **41**, 601 (1990).
24. M. D. Hürlimann, *J. Magn. Reson.* **152**, 109 (2001).
25. M. H. Levitt, R. Freeman, T. Frenkiel, *Adv. Magn. Reson.* **11**, 47 (1983).
26. R. Tycko, *Phys. Rev. Lett.* **51**, 775 (1983).

26 March 2002; accepted 15 May 2002

Direct Measurement of the Reaction Front in Chemically Amplified Photoresists

Eric K. Lin,[1]* Christopher L. Soles,[1] Dario L. Goldfarb,[3] Brian C. Trinque,[4] Sean D. Burns,[4] Ronald L. Jones,[1] Joseph L. Lenhart,[1] Marie Angelopoulos,[3] C. Grant Willson,[4] Sushil K. Satija,[2] Wen-li Wu[1]

The continuing drive by the semiconductor industry to fabricate smaller structures using photolithography will soon require dimensional control at length scales comparable to the size of the polymeric molecules in the materials used to pattern them. The current technology, chemically amplified photoresists, uses a complex reaction-diffusion process to delineate patterned areas with high spatial resolution. However, nanometer-level control of this critical process is limited by the lack of direct measurements of the reaction front. We demonstrate the use of x-ray and neutron reflectometry as a general method to measure the spatial evolution of the reaction-diffusion process with nanometer resolution. Measuring compositional profiles, provided by deuterium-labeled reactant groups for neutron scattering contrast, we show that the reaction front within the material is broad rather than sharply defined and the compositional profile is altered during development. Measuring the density profile, we directly correlate the developed film structure with that of the reaction front.

The tremendous device performance increases by the semiconductor industry have been driven by the successful development of materials and tools for the high-volume fabrication of smaller device structures with photolithography. By 2003, the semiconductor industry predicts that structures with sub–100-nm critical dimensions will be needed (*1*), but many difficult materials challenges remain. The critical dimension must be controlled over 2 to 5 nm length scales, which is comparable to the characteristic size of the polymeric molecules in the photoresists used to pattern the features (*2*). Furthermore, thinner photoresist films are required because of increasing optical absorption with decreasing imaging wavelengths. Thinner photoresist films and the production of nanoscale structures can involve changes in key photoresist properties from those of the bulk material (*3*–*6*). Quantitative measurements of material

[1]Polymers Division and [2]Center for Neutron Research, National Institute of Standards and Technology, Gaithersburg, MD 20899–8541, USA. [3]IBM T. J. Watson Research Center, Yorktown Heights, NY 10598, USA. [4]Departments of Chemistry and Chemical Engineering, University of Texas at Austin, Austin, TX 78712, USA.

*To whom correspondence should be addressed. E-mail: eric.lin@nist.gov

and transport properties in thin resist films with nanometer resolution are critical to the understanding, development, and control of the processes needed to fully realize sub–100- nm lithography.

State-of-the-art semiconductor devices with 130-nm dimensions are fabricated using chemically amplified (CA) photoresists. In particular, a positive tone CA photoresist consists of a polymer with an acid-labile pendant protection group, photoacid generator molecules (PAG), and other additives (*7*–*9*). Upon exposure to radiation through a patterned mask, the PAG undergoes a photochemical reaction that generates a low concentration of acid. During a post-exposure bake (PEB), the acid diffuses and catalyzes a deprotection reaction that cleaves the pendant group of the insoluble polymer, resulting in a polymer that is soluble in the developer. The term amplification refers to the ability of a single acidic proton to catalyze hundreds of deprotection events under standard processing conditions (*10*). As a result, a CA photoresist is very sensitive and requires only low exposure doses and enables very fine resolution. There is a balance, however; the acid must be mobile enough within the polymer matrix to deprotect large numbers of pendant groups, yet excessive diffusion leads to image blur and poor resolution. The ultimate resolution of a CA photoresist is a complex function of several related parameters, including the mobility of the acidic proton and the deprotection reaction kinetics. Questions remain about acid diffusion mechanisms, their dependence on the local chemical environment, and the final development process. The spatial evolution of the deprotection reaction within the material and the compositional dependence of the development process have not been measured with sufficient spatial resolution (*11*–*16*) to distinguish between reaction-diffusion models (*17*–*21*) nor to test their applicability for the fabrication of sub–100-nm structures.

We directly measure the reaction front profile before and after development through complementary x-ray (XR) and neutron reflectivity (NR) measurements on model bilayer structures. We present quantitative data about the spatial evolution of the reaction front into a photoresist material and the relation between the reaction front and the final developed structure. These measurements were enabled by synthesizing a photoresist polymer with a deuterium-substituted protection group. The deuterium provides strong contrast in neutron reflectivity without changing the chemistry of the system. As a result, we were able to measure both compositional and density profiles after varying processing conditions with nanometer resolution.

Bilayer structures were prepared on cleaned silicon wafers primed with hexamethyldisilazane (HMDS) vapor. Figure 1 schematically shows the steps used to prepare the bilayers that correspond to standard photoresist processing conditions. Specular reflectivity ($I_{reflected}/I_{incident}$) measurements were used to determine both the compositional and density depth profiles of the bilayer structure (*22*). X-ray reflectivity measurements were performed on modified x-ray diffractometers with fine focus x-ray tubes with a wavelength (λ) of 1.54 Å. Neutron reflectivity measurements were performed on the NG7 reflectometer at the National Institute of Standards and Technology Center for Neutron Research, using a neutron λ of 4.75 Å. The logarithm of the reflectivity is plotted as a function of the scattering vector, q [$q = (4\pi/\lambda)\sin\theta$; θ is the incident and detector angle]. The scattering vector is perpendicular to the sample surface, providing planar-averaged depth profile information. Depth profiles in scattering contrast are determined from fitting the reflectivity data to model profiles, calculating their reflectivity using the recursive multilayer method, and iterating with a least-squares regression algorithm (*23*).

Compositional and density profiles can be determined from the same sample because of differences in the interaction of x-ray and neutron radiation with matter. X-rays are scattered by differences in electron density. p-*tert*-butoxycarboxystyrene (PBOCSt) and poly(hydroxystyrene) (PHOSt) have very similar densities (low x-ray contrast), and overall density profiles are obtained. In contrast, neutrons are scattered by nuclear interactions. There is a large and convenient difference in the neutron scattering cross section between deuterium and hydrogen nuclei, providing strong contrast with slight chemical modification (*24*).

The deprotection reaction during the PEB step is generally written as shown in Fig. 2 (*7*, *25*). Although a complete description of the deprotection reaction involves other byproducts and side reactions (*26*), nearly all of the reaction products from the cleaved deuterated protection group, including CO_2 and isobutylene (d_8), are gaseous and rapidly evolve from the sample (*27*, *28*). Some side reactions

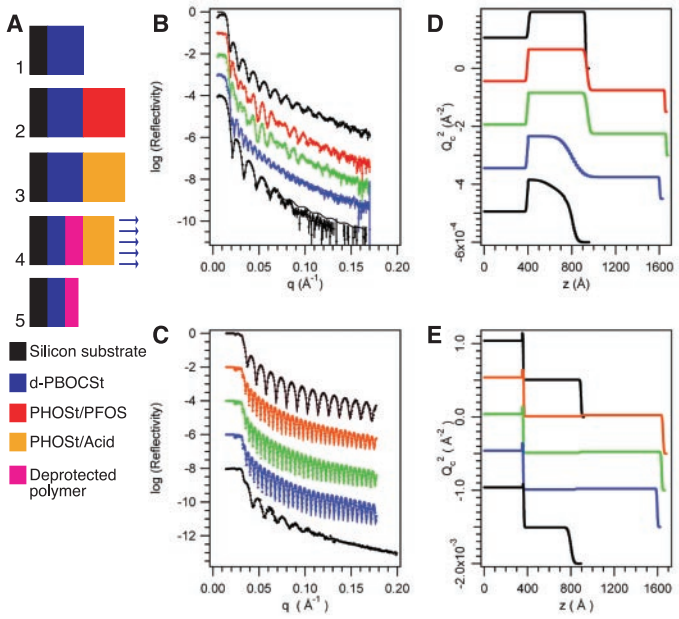

Fig. 1. (**A**) Schematic of the geometry of the bilayer samples and the effects of each of the five processing steps. In step 1, the lower layer consisting of the deuterium-labeled protected polymer, d-PBOCSt number average relative molecular mass ($M_{r,n}$) and weight average ($M_{r,w}$) and [$M_{r,n}$ = 21000, $M_{r,w}/M_{r,n}$ = 2.1] was spin-coated from a propylene glycol methyl ether acetate (PGMEA) solution and baked (PAB) for 90 s on a 130°C hotplate to remove residual solvent (*35*). The d-PBOCSt was synthesized by protecting PHOSt with a deuterium-substituted (di-*tert*-dicarbonate d_{18}) group (*34*, *36*). In step 2, the upper layer was spin-coated from a 1-butanol solution directly onto the lower layer; this upper layer consisted of PHOSt ($M_{r,n}$ = 5260, $M_{r,w}/M_{r,n}$ = 1.12), the corresponding deprotected polymer, loaded with a 5% mass fraction of the PAG, PFOS. The bilayer is subjected to another PAB for 90 s at 130°C. In step 3, the bilayer stack was exposed with a dose of 1000 mJ/cm^2 to broadband UV radiation to generate acid within the top PHOSt layer. In step 4, a PEB was applied for 90 s at 110°C to initiate and propagate the reaction-diffusion process from the PHOSt layer into the d-PBOCSt layer. Lastly, in step 5, the original PHOSt layer and the soluble deprotected d-PBOCSt reaction products were removed (developed) by immersion in a 0.26 N tetramethylammonium hydroxide (TMAH) solution for 30 s, followed by a rinse with deionized water. Neutron reflectivity (**B**) and x-ray reflectivity (**C**) data and the best fits to the data corresponding to samples processed after each processing step. The curves are vertically offset for clarity. Real space profiles in terms of the neutron (**D**) or x-ray (**E**) elastic coherent scattering density corresponding to the best fits to the experimental data in (B) and (C). The curves are vertically offset for clarity. The abscissa origin is within the silicon wafer and moves into the d-PBOCSt and PHOSt layers.

may include the attachment of deuterium-labeled groups to the deprotected polymer, but the fraction of these events is small relative to the general pathway shown (*26*). The removal of volatile deuterated reaction products changes the neutron scattering contrast of the remaining material proportional to the local extent of reaction.

In Fig. 1, B and C, NR and XR data, respectively, are shown along with the best fits at each processing step. The data were taken from separate, identically prepared samples to minimize delay effects between processing steps (*7*). The oscillations in the reflectivity data result from constructive and destructive interference of the incident radiation reflected from interfaces in the bilayer. The periodicity, amplitude, and decay rate of the reflectivity data are sensitive to structural features of the depth profile such as layer thickness, composition or density, and interfacial width (*22*, *29*). The real space depth profiles corresponding to the best fits are shown in Fig. 1, D and E, in terms of the elastic coherent scattering per unit volume, Q_c^2, a quantity proportional to the elemental composition and the material density.

In step 1, the initial thickness of the deuterated PBOCSt (d-PBOCSt) layer was 534 ± 1 Å with a surface roughness of 13 ± 1 Å (*30*). At step 2, the thickness of the PHOSt layer with di(*tert*-butylphenyl) iodonium perfluorooctanesulfonate (PFOS) was 717 ± 1 Å. The interfacial width between the two layers broadened slightly to 40 ± 1 Å without any change in the nominal d-PBOCSt thickness, as there is very little intermixing between the layers after spin-coating. After the ultraviolet (UV) exposure, there was no change at the bilayer interface. However, after the PEB, there was a change in the NR curve due to dramatic changes in the interfacial compositional profile. Control experiments on identical bilayers without PFOS in the PHOSt layer confirm that the interfacial width between d-PBOCSt and PHOSt was unaffected by these processing conditions. The observed interfacial broadening is due to propagation of the acid-catalyzed reaction front and not thermal deprotection.

To facilitate further discussion, we plot compositional and density profiles of selected samples normalized to either d-PBOCSt fraction (NR, dotted lines, left axis, Fig. 3) or material volume fraction (XR, solid line, right axis, Fig. 3). Figure 3A compares the compositional profiles of the initial bilayer and the reaction front after the PEB. In the initial bilayer, the interface between d-PBOCSt and PHOSt was narrow. After the bake, the reaction front propagated into the d-PBOCSt layer, and the compositional interface broadened due to the deprotection events. Although we cannot directly determine the PFOS distribution at the bilayer interface during step 2, the interfacial broadening and coincidence of the beginning of the reaction front and the initial bilayer interface suggest that the initial PFOS distribution is not an issue. Preliminary experiments show that the reaction front broadens with time, indicating that PFOS is not distributed through the PBOCSt layer.

The interfacial transition between the d-PBOCSt and PHOSt layers at step 4 can be modeled with an error function with an interfacial width of 190 ± 5 Å. The reaction front does not remain sharply defined (corresponding to the initial bilayer interface) but instead broadens, thus narrowing the number of possible reaction-diffusion descriptions for this process. Although a simple error function is able to fit the reaction front profile, the reaction-diffusion process is considerably more complex (*7*, *16*, *17*). In similar systems, it has been shown that the extent of reaction is fast at short times and then saturates at longer times (*5*, *12*, *16*). In addition, the loss of material during the deprotection reaction dynamically changes both the local acid concentration and chemical composition. Other factors include the production of volatile products that may alter the acid diffusion process, the rate dependence of the reaction on acid-base equilibrium and/or local concentration, and the effects of additives in the photoresist formulation. Descriptions of the reaction-diffusion process have included these factors, but have not been validated directly with the spatial evolution of the reaction front (*17*, *18*). These data provide a stringent test for any proposed simulation or model calculation for the reaction front propagation and can be used to screen and evaluate different approaches quantitatively. NR and XR studies of the reaction profile evolution with bake time and temperature are necessary to fully understand this complex process.

In step 5, an aqueous base was used to remove both the original PHOSt acid feeder layer as well as soluble products from the deprotection of d-PBOCSt. Using XR, we are able to correlate the spatial extent of the reaction front within the sample with the developed structure. Figure 3B compares the compositional profiles of the reaction front after the PEB and after development. After development, the compositional profile from step 4 is further altered, and the compositional profile in step 5 can no longer be described with an error function. Model reflectivity calculations of profiles

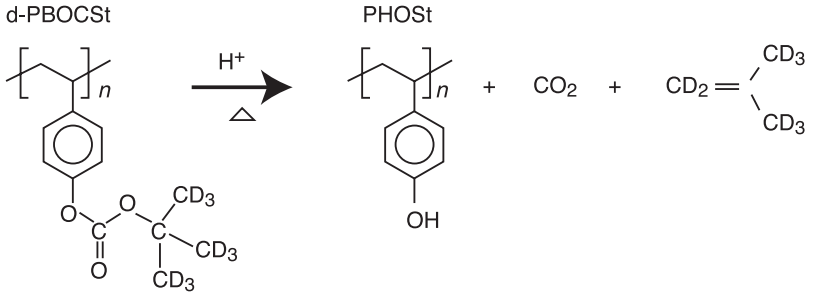

Fig. 2. The general acid-catalyzed deprotection reaction during the PEB.

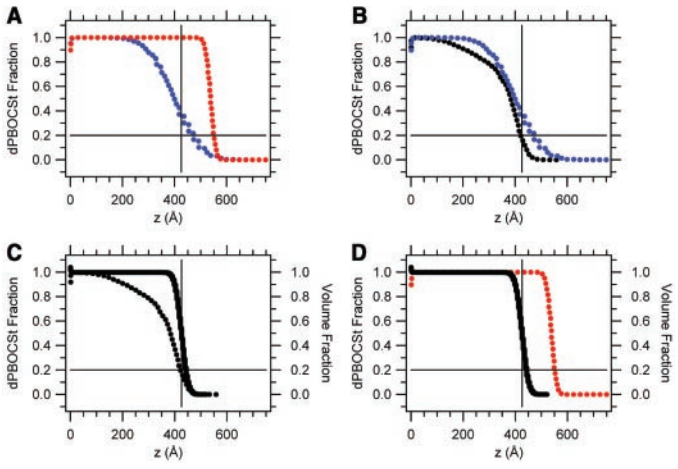

Fig. 3. Comparisons between compositional profiles (d-PBOCSt mass fraction, dotted lines) and density profiles (material volume fraction, solid line) plotted as a function of distance from the silicon surface after varying processing steps. The horizontal lines represent the accepted value of approximately 80% conversion needed for solubility to the developer. The vertical lines represent the location of the thickness of the final developed structure as measured by x-ray reflectivity. (**A**) Compositional profiles of the initial bilayer interface (red) and the reaction front profile (blue). (**B**) Compositional profiles of the reaction front (blue) and the developed structure (black). (**C**) Compositional profile (dotted) and the volume fraction profile (solid) of the developed structure. (**D**) Compositional profile of the initial bilayer interface (red) and the final developed volume fraction profile (black).

generated by removing sections with greater than 80% deprotection from step 4 cannot fit the experimental reflectivity data. In addition, the developer removes 12 ± 2% of the remaining deuterated material from step 4. This is not unexpected because copolymers with a composition of less than 20% protection level are generally soluble in the base developer (*31*). There are several possible explanations for the changing compositional profile. First, the polydispersity of the d-PBOCSt used in this study is significant and the removal of material could arise from the loss of polymers with lower relative molecular masses as fewer deprotection events are needed to effect solubility of smaller polymers (*32*). Second, the profile change may arise from rearrangement of the surface material from the development process. The developer solution could swell the surface layer enough to impart sufficient mobility to change the compositional profile. Lastly, there may be some reaction products with deuterium-labeled parts that are soluble in the developer.

In Fig. 3C, we compare the compositional and density profiles of the developed structure, and, in Fig. 3D, we compare the compositional profile of the initial bilayer with the volume fraction profile of the developed structure. The thickness of the developed d-PBOCSt layer (step 5) from XR was 433 ± 1 Å and the surface roughness was 47 ± 4 Å, nearly identical to the width of the initial bilayer interface even though the interfacial width of the reaction front was nearly 200 Å wide. If the developed structure was used to infer information about the reaction-diffusion process, then one could conclude that the reaction front propagates over a distance of 100 Å as a sharply defined band into the d-PBOCSt layer (*33*). The sensitivity to composition of the deprotected polymer solubility in the developer is responsible for the possible fabrication of well-defined nanostructures with diffusive transport mechanisms.

More insight can be obtained from comparisons with accepted design criteria for development in this resist system. The horizontal lines in Fig. 3 show the 80% deprotection level generally accepted as the solubility transition. At this deprotection level, the thickness of the developed layer from the buried reaction front profile was 464 ± 5 Å, whereas the final film thickness was 433 ± 1 Å. Even with an accurate prediction of the reaction front profile, the development step can change the predicted line width. The 30 Å difference between the position of the reaction front and the final developed structure is a large fraction of the anticipated error budget for sub–100-nm feature fabrication. The vertical lines in Fig. 3 show the thickness of the final film defined as the midpoint of the interfacial roughness. At this thickness, the deprotection level in the buried reaction front (step 4) is 67 ± 5%, suggesting that the solubility composition limit is lower than expected. However, the deprotection level at the surface of the developed film (step 5) is very close to the expected 80% level. The removal of additional material is responsible for the bias toward smaller structures than that predicted from the reaction front profile alone. Although examination of the final structure validates accepted design rules, comparison with the buried reaction front shows that both the reaction-diffusion and development process require investigation, especially for the fabrication of sub–100-nm structures. For example, the breadth of the reaction front shown here could encompass an entire line width. Actual fabrication of sub–100-nm lines would involve two opposing reaction fronts that may interact and affect the dimensions of the patterned structure. For the fabrication of sharply defined features, dimensional control will require detailed information about both the reaction front profile and the development process.

We have demonstrated the use of x-ray and neutron reflectometry as a general method to obtain quantitative, detailed information about the spatial evolution of the reaction-diffusion process in chemically amplified photoresists. Through isotopic labeling, we can obtain both compositional and density profiles with nanometer resolution, and this can be readily extended to other photoresist systems. Data sets from different material formulations and compositions and a range of processing conditions can be used to identify the fundamental chemical and transport mechanisms governing the fabrication of sub–100-nm devices, and they can also be used to quantitatively measure physical parameters needed to develop and validate advanced photolithography simulation software used to design these processes.

References and Notes

1. *2001 National Technology Roadmap for Semiconductors* (The Semiconductor Industry Association, San Jose, CA, 2001).
2. G. M. Schmid *et al.*, *Proc. SPIE* **4345**, 1037 (2001).
3. C. W. Frank *et al.*, *Science* **273**, 912 (1996).
4. C. L. Soles *et al.*, *J. Vac. Sci. Technol.* **B19**, 2690 (2001).
5. D. L. Goldfarb *et al.*, *J. Vac. Sci. Technol.* **B19**, 2699 (2001).
6. D. S. Fryer, P. F. Nealey, J. J. de Pablo, *Macromolecules* **33**, 6439 (2000).
7. H. Ito, C. G. Willson, *Polym. Eng. Sci.* **23**, 1021 (1982).
8. J. Frechet, H. Ito, C. G. Willson, *Proc. Microcircuit Eng.* **82**, 260 (1982).
9. G. M. Wallraff, W. D. Hinsberg, *Chem. Rev.* **99**, 1801 (1999).
10. D. R. McKean, U. Schaedeli, S. A. MacDonald, *J. Polym. Sci. A* **27**, 3927 (1989).
11. T. H. Fedynyshyn *et al.*, *J. Vac. Sci. Technol.* **B12**, 3888 (1994).
12. T. Itani *et al.*, *J. Vac. Sci. Technol.* **B14**, 3026 (1995).
13. J. B. Kim *et al.*, *Polymer* **40**, 1087 (1999).
14. B. Lu *et al.*, *J. Vac. Sci. Technol.* **B17**, 3345 (1999).
15. S. V. Postnikov *et al.*, *J. Vac. Sci. Technol.* **B17**, 3335 (1999).
16. M. D. Stewart *et al.*, *Proc. SPIE* **3999**, 665 (2000).
17. F. A. Houle *et al.*, *J. Vac. Sci. Technol.* **B18**, 1874 (2000).
18. M. Zuniga, A. R. Neuteuther, *J. Vac. Sci. Technol.* **B13**, 2957 (1995).
19. J. S. Peterson *et al.*, *Proc. SPIE* **2438**, 167 (1995).
20. A. A. Krasnoperova *et al.*, *J. Vac. Sci. Technol.* **B12**, 3900 (1994).
21. E. Croffie, M. Cheng, and A. Neureuther, *J. Vac. Sci. Technol.* **B17**, 3339 (1999).
22. T. P. Russell, *Mater. Sci. Rep.* **5**, 171 (1990).
23. L. G. Parratt, *Phys. Rev.* **95**, 359 (1954).
24. J. S. Higgins, H. C. Benoit, *Polymers and Neutron Scattering* (Oxford Univ. Press, New York, 1994).
25. Time-resolved Fourier-transformed infrared measurements of the reaction kinetics of PBOCSt films loaded with PAG after UV exposure and during PEB show little difference between identically synthesized deuterated and hydrogenated PBOCSt.
26. H. Ito, M. Sherwood, *Proc. SPIE* **3678**, 104 (1999).
27. F. A. Houle *et al.*, *Proc. SPIE* **3999**, 181 (2000).
28. S. D. Burns *et al.*, in *Forefront of Lithographic Materials Research*, H. Ito, M. M. Khojasteh, W. Li, Eds., 12th International Conference on Photopolymers, McAfee, NJ, October 2000 (Society of Plastics Engineers, Brookfield, CT, 2001), pp. 323–334.
29. When possible, an error function is used to describe interfacial transitions. The reported interfacial widths are defined as 2σ, where σ is the standard deviation of the Gaussian width of the error function.
30. The data in the figures and in the text are presented along with the standard uncertainty of the measurement.
31. H. Ito, *J. Photopolym. Sci. Technol.* **11**, 379 (1998).
32. P. C. Tsiartas *et al.*, *Macromolecules* **30**, 4656 (1997).
33. A sharply defined reaction front was observed in a similar bilayer system with scanning electron microscopy (SEM) measurements of the deprotected polymer (*16*). SEM samples were prepared by cleaving a bilayer sample stack, silylating the PHSOSt polymer, etching with oxygen plasma, and then coating with gold and/or palladium. However, the smallest observable length scales are larger than those of the reflectivity techniques, the silylation reaction sensitivity to deprotection composition is not known, and much longer diffusional times and distances were used.
34. B. M. Pope, Y. Yamamoto, D. S. Tarbell, *Org. Synth.* **6**, 418 (1988).
35. During the post-apply baked (PAB) and PEB, the surface temperature of the silicon wafer (<111> orientation, 3 mm thick, 75 mm diameter) reaches a steady state value approximately 5 to 10°C lower than the set point temperature. The steady state temperature is reached after nearly 30 s.
36. d-PBOCSt was synthesized by a procedure, as follows: 2-methyl-2-propanol-d_{10} was reacted with 1 equivalent potassium metal in dry tetrahydrofuran (THF) to form potassium tert-butoxide-d_9. The reaction was considered to be complete when all of the potassium appeared to dissolve in the THF; this generally took about 48 hours at reflux temperature. This salt was then used as starting material for the published literature procedure for di-*tert*-butyl dicarbonate (*34*). 1.1 Equivalents of di-*tert*-butyl dicarbonate-d_{18} were reacted with PHOSt with 0.1 equivalents 4-(dimethylamino)pyridine in dry THF. Precipitation into hexanes afforded a 95% yield of a white polymer that was 92% protected as measured with thermogravimetric analysis (TGA).

37. Supported by the Defense Advanced Research Projects Agency under grant N66001-00-C-8803. We also thank T. Mrozek and D. Medeiros for their insight and helpful discussion. J.L.L. acknowledges support through the National Research Council–National Institute of Standards and Technology Postdoctoral Fellowship Program.

21 March 2002; accepted 12 June 2002